

Novel Magnetic Quantization of sp^3 Bonding in Monolayer Tinene

Szu-Chao Chen¹, Chung-Lin Wu², Jhao-Ying Wu^{2,*}, and Ming-Fa Lin^{2,*}

¹Center for Micro/Nano Science and Technology, National Cheng Kung University, Tainan, Taiwan 701

²Department of Physics, National Cheng Kung University, Tainan, Taiwan 701

A generalized tight-binding model, which is based on the subenvelope functions of the different sublattices, is developed to explore the novel magnetic quantization in monolayer gray tin. The effects due to the sp^3 bonding, the spin-orbital coupling, the magnetic field and the electric field are simultaneously taken into consideration. The unique magneto-electronic properties lie in two groups of low-lying Landau levels, with different orbital components, localization centers, state degeneracy, spin configurations, and magnetic- and electric-field dependences. The first and second groups mainly come from the $5p_z$ and $(5p_x, 5p_y)$ orbitals, respectively. Their Landau-level splittings are, respectively, induced by the electric field and spin-orbital interactions. The intragroup anti-crossings are only revealed in the former. The unique tinene Landau levels are absent in graphene, silicene and germanene.

PACS:

I. INTRODUCTION

The layered group-IV condensed-matter systems have attracted enormous attention,^{1–9} mainly owing to their nano-scaled thickness and hexagonal symmetry. They are ideal two-dimensional (2D) materials for studying novel physical, chemical and material phenomena,^{1–6,10–16} and they have high potential for technical applications^{4,7,17,18} in the near future. Graphene, with the strong sp^2 bonding in the one-atom-thick plane, was the first stable 2D crystal produced by mechanical exfoliation in 2004.¹ Its Si and Ge counterparts, silicene and germanene, have been synthesized on metallic substrates.^{7,8,19–22} Recently, a single layer of Sn atoms, tinene, has been fabricated on a substrate of bismuth telluride.⁹ Silicene, germanene and tinene have low-buckled structures (Fig. 1(b)) with a mixed sp^2 - sp^3 hybridization rather than a sp^2 one, since the relatively weak chemical bonding between the larger atoms cannot maintain a planar structure. Furthermore, the spin-orbital coupling (SOC) is evidently stronger than that of graphene and can open an energy gap. The effects of the sp^3 bonding and SOC are pronounced in silicene and germanene and are expected to become even more significant in tinene. The magnetic quantization in tinene will be investigated by using the generalized tight-binding model,^{23–25} in which all the critical interactions are taken into account simultaneously. Comparison with the other 2D systems is also made.

The hexagonal symmetry causes graphene to exhibit a pair of linear (π, π^*) bands intersecting at the Fermi level ($E_F = 0$) near the corners of the hexagonal Brillouin zone (K and K' in the inset of Fig. 2(a)). However, the SOC slightly separates two Dirac points and modifies the energy dispersions in silicene and germanene. Their low-energy π -electronic structures could be well described by the effective-mass model,²⁶ being consis-

tent with the first-principles calculations.¹⁴ On the other hand, tinene has the strong sp^3 bonding and SOC, leading to the low-lying π and σ bands formed by the $5p_z$ and $(5p_x, 5p_y)$ orbitals, respectively. These special low-energy bands are expected to enrich the magnetic quantization.

A uniform perpendicular magnetic field ($\mathbf{B}_z = B_z \hat{z}$) makes electronic states flock together and induces many Landau levels (LLs). For graphene, silicene and germanene, the low-lying π -electronic states can be directly quantized by the effective-mass model. The LL energies are approximated by a square-root form $E^{c,v} = \text{sgn}(n^{c,v}) \sqrt{(-\frac{1}{2}\xi\eta\Delta_{so})^2 + 2|n^{c,v}|v_F^2\hbar eB_z/c}$, where c represents the conduction state, v the valence state, $n^{c,v}$ the LL quantum mode, $\xi = \pm 1$ the K or K' valley index, $\eta = \pm 1$ the spin index, Δ_{so} the spin-orbital band gap, and v_F the Fermi velocity.^{10–12} The $\sqrt{B_z}$ -dependent LL energies in graphene with $\Delta_{so} = 0$ have been confirmed by scanning tunneling spectroscopy (STS)^{27,28} and magneto-optical experiments of cyclotron resonance.²⁹ Specially, the stronger SOC's in silicene and germanene lead to the splitting of the $n^{c,v} = 0$ LL with energy spacing Δ_{so} .^{11–13}

The effective-mass model may be too cumbersome or complex to study the magneto-electronic properties of monolayer tinene with its strong sp^3 bonding and SOC, although it could conceivably be used to comprehend the low-energy magnetic quantization of graphene, silicene and germanene. Apparently, the feature-rich energy bands of tinene, with multi-valley structures near E_F ,¹⁵ cause huge difficulties in directly diagonalizing the magnetic Hamiltonian matrix. We will develop the generalized tight-binding model for various orbital hybridizations, spin configurations, and external fields, in which the Hamiltonian matrix is built from the orbital- and spin-dependent tight-binding basis functions. The spatial distributions of the subenvelope functions on the distinct sublattices are critical

for distinguishing the main features of LLs. This study shows that monolayer tinene exhibits a novel magnetic quantization. Two groups of LLs, which are dominated by the $5p_z$ and $(5p_x, 5p_y)$ orbitals, respectively, have distinct localization centers, orbital components, spin configurations, state degeneracies, and magnetic- and electric-field dependences. The predicted LL energy spectra can be verified by STS measurements.³⁰

II. METHODS

The generalized tight-binding model is further developed to include the sp^3 orbital bonding, the SOC, and the electric and magnetic fields simultaneously. Tinene consists of two equivalent A and B sublattices, respectively, located at two parallel planes with a separation of l_z (0.417 Å). The primitive unit vectors are \mathbf{a}_1 and \mathbf{a}_2 with a lattice constant of $a=4.7$ Å (Fig. 1(a)), and the angle between the Sn-Sn bond and the z -axis is $\theta = 107.1^\circ$ (Fig. 1(b)). The $5s$ orbital energy is $E_s = -6.2335$ eV below that of the $5p$ orbitals taken as zero ($E_p = 0$). The Slater-Koster hopping parameters in the sp^3 bonding are $V_{ss\sigma} = -2.6245$ eV, $V_{sp\sigma} = 2.6504$ eV, $V_{pp\sigma} = 1.4926$ eV, and $V_{pp\pi} = -0.7877$ eV (Fig. 1(c)). The SOC strength ($\lambda_{soc} = 0.8$ eV) of tinene is predicted to be two orders of magnitude greater than that of graphene.^{31,32} This interaction under the Coulomb central potential, $V_{soc} = \lambda_{soc} \vec{L} \cdot \vec{s}$, will induce dramatic changes in electronic properties. Here, V_{soc} corresponds to the same atom and only the $5p$ orbitals contribute to V_{soc} . In the bases of $\{|5p_z^A\rangle, |5p_x^A\rangle, |5p_y^A\rangle, |5s^A\rangle, |5p_z^B\rangle, |5p_x^B\rangle, |5p_y^B\rangle, |5s^B\rangle\} \otimes \{\uparrow, \downarrow\}$, the nearest-neighbor Hamiltonian is expressed as

$$H = \sum_{\langle i \rangle, o, m} E_o C_{iom}^+ C_{iom} + \sum_{\langle i, j \rangle, o, o', m} \gamma_{oo'}^{\mathbf{R}_{ij}} C_{iom}^+ C_{jo'm} + \sum_{\langle i \rangle, p_\alpha, p_\beta, m, m'} \frac{\lambda_{SOC}}{2} C_{ip_\alpha m}^+ C_{ip_\beta m'} (-i\epsilon_{\alpha\beta\gamma} \sigma_{mm'}^\gamma),$$

where $i(j)$, $o(o')$, and $m(m')$ stand for the lattice site, atomic orbital, and spin, respec-

tively. The first and second terms are, respectively, the site energy (E_o) and the nearest-neighbor hopping integral ($\gamma_{oo'}^{\mathbf{R}_{ij}}$). The latter depends on the type of atomic orbitals, the translation vector of the nearest-neighbor atom (\mathbf{R}_{ij}), and θ . The sufficiently strong sp^3 hybridization not only gives rise to the hoppings between $5p_z$ and $(5p_x, 5p_y, 5s)$ orbitals, e.g., $\gamma_{zx}^{\mathbf{R}_1} = (V_{pp\pi} - V_{pp\sigma}) \sin \theta \cos \theta$, but also leads to the misorientation of $p\pi$ orbitals ($\gamma_{zz}^{\mathbf{R}_{ij}} = V_{pp\pi} \sin^2 \theta + V_{pp\sigma} \cos^2 \theta$).³³ For the planar case ($\theta = 90^\circ$), $|5p_z\rangle$ is orthogonal to $(|5p_x\rangle, |5p_y\rangle, |5s\rangle)$ and there are only $p\pi$ bondings in parallel $5p_z$ orbitals. The last term represents the V_{soc} on the same atom where α, β and γ , respectively, denote the x, y and z components, and σ is the Pauli spin matrix. The V_{soc} between $|5p_x\rangle$ and $|5p_y\rangle$ results in the splitting of states with opposite spin configurations, while that between $|5p_z\rangle$ and $|5p_x\rangle$ ($|5p_y\rangle$) leads to the splitting of states and an interchange of spin configurations.

In a uniform perpendicular magnetic field, the \mathbf{B}_z -induced periodical Peierls phases can modulate the hopping integral as $\gamma_{oo'}^{\mathbf{R}_{ij}}(\mathbf{B}_z) = \gamma_{oo'}^{\mathbf{R}_{ij}} \exp i(\frac{2\pi}{\Phi_0} \int_{r_j}^{r_i} \mathbf{A}(\mathbf{r}) \cdot d\mathbf{r})$, where Φ_0 (hc/e) is the flux quantum. In the Landau gauge $\mathbf{A} = (0, B_z x, 0)$, the unit cell becomes an enlarged rectangle with $4R_B$ ($4 \times 21665/B_z$) atoms (Fig. 1(a)), where R_B is the ratio of Φ_0 versus magnetic flux through each hexagon. The reduced Brillouin zone has an area of $4\pi^2/\sqrt{3}a^2R_B$. The magnetic Hamiltonian is built from the space spanned by the $32R_B$ tight-binding functions $\{|A_{om}^i\rangle; |B_{om}^i\rangle |i = 1, 2, \dots, 2R_B; o = 5p_x, 5p_y, 5p_z, 5s; m = \uparrow, \downarrow\}$, related to the i th A and B atoms in the rectangular unit cell. An electric field along the z -axis introduces a potential energy $V_z/2$ ($-V_z/2$) to the site energy of the A (B) sublattice. Due to the sp^3 hybridization, the hopping integrals of the three nearest neighbors might have different signs, e.g., $\gamma_{xy}^{\mathbf{R}_2} = -\gamma_{xy}^{\mathbf{R}_3}$, which means the corresponding matrix elements are complex for any wavevectors (\mathbf{k}' s). In our calculations, the $32R_B \times 32R_B$ Hermitian matrix

is transformed into a band-like matrix, in which the base functions are arranged in a specific sequence²³ $\{|A_{om}^1\rangle, |B_{om}^{2R_B}\rangle, |B_{om}^1\rangle, |A_{om}^{2R_B}\rangle, |A_{om}^2\rangle, |B_{om}^{2R_B-1}\rangle, |B_{om}^2\rangle, |A_{om}^{2R_B-1}\rangle \dots\}$. Numerical diagonalization for solving the eigenvalues ($E^{c,v'l}s$) and eigenfunctions ($\Psi^{c,v'l}s$) is more efficient. The generalized tight-binding model could be further employed to comprehend the magnetic quantization in other layered systems with complex orbital bonding and spin configurations.

III. RESULTS AND DISCUSSION

Tinene has feature-rich energy bands, mainly owing to the critical SOC and sp^3 bonding. Two pairs of energy bands, out of a total of four, lie near E_F . In this two pairs, each electronic state is doubly degenerate for the spin degree of freedom. Without the SOC (black curves in Fig. 2(a)), one pair of linear bands intersects at the K (K') point, and two pairs of parabolic bands appear near the Γ point because of the strong sp^3 bonding. The former and the latter mainly originate from the $5p_z$ and $(5p_x, 5p_y)$ orbitals, respectively (Figs. 2(b) and 2(c)). V_{SOC} further induces the anti-crossing of energy bands and the splitting of degenerate states (green curves). At the K (K') point, the Dirac point is separated, and the doubly degenerate wavefunctions of the first valence band are dominated by $|5p_z^B; \downarrow\rangle$ and $|5p_z^A; \uparrow\rangle$ ($|5p_z^B; \uparrow\rangle$ and $|5p_z^A; \downarrow\rangle$), where only the first degenerate state is shown (black curves in Fig. 2(b)). Along $K \rightarrow M$ ($K' \rightarrow \Gamma$), the contribution of $|5p_z^B; \downarrow\rangle$ ($|5p_z^B; \uparrow\rangle$) quickly declines, while the opposite is true for that of $|5p_z^A; \downarrow\rangle$ ($|5p_z^A; \uparrow\rangle$). For the first conduction band, the $5p_z$ -dependent wavefunction exhibits similar behavior under the interchange of the two sublattices (Fig. 2(c)). These results imply that the π - and

π^* -electronic states strongly depend on the spin configurations and the two sublattices. On the other hand, in the vicinity of the Γ point, the state degeneracy is lifted by the V_{SOC} between $5p_x$ and $5p_y$ orbitals, and one of the parabolic bands is close to E_F . An indirect energy gap, which corresponds to the highest occupied state at the Γ point and the lowest unoccupied state at the K point, is about 54 meV. In addition, the anti-crossings along $\Gamma \rightarrow K'$ ($\Gamma \rightarrow M$) are attributed to the V_{SOC} of the $5p_z$ and $(5p_x, 5p_y)$ orbitals. $|\Psi^{v1}(\Gamma)|^2$ has almost the same weight on the A and B sublattices, but the spin-up state is much stronger than the spin-down state. Along $\Gamma \rightarrow K'$ ($\Gamma \rightarrow M$), $|\Psi^{v1}(\mathbf{k})|^2$ is dominated by the spin-up states (spin-up and spin-down states). That is to say, the spin configurations are anisotropic. Tinene possesses special low-lying energy bands quite different from the linear ones of graphene, silicene and germanene. It therefore exhibits rich magnetic quantization. It should also be noted that the tight-binding model calculations are consistent with the first-principles ones.¹⁵

Tinene has two groups of well-behaved low-lying LLs, in which the valence and conduction LLs of each group are asymmetric about E_F (Figs. 3(a) and 3(c)). The first and second groups, respectively, correspond to the magnetic quantization of the electronic states near the K (K') and Γ points. For each (k_x, k_y) , the LLs of the former are eight-fold degenerate, except for the initial valence and conduction ones, being attributed to the K and K' valleys, the mirror symmetry of $z = 0$ plane, and the spin degree of freedom. At $(k_x = 0, k_y = 0)$, the degenerate states are localized at the 1/6, 2/6, 4/6 and 5/6 positions of the enlarged unit cell. The 2/6 (1/6) states, analogous to the 5/6 (4/6) ones, originate from the electronic states in the K (K') valley. On the other hand, the LLs of the second group are doubly degenerate, since there is only one Γ valley, and the V_{SOC} between the $5p_x$ and $5p_y$

orbitals leads to distinct spin-dominated LL states (Fig. 3(d)). The two degenerate states are similar but localized at the 0 and 1/2 positions of the enlarged unit cell. In addition, the carrier density, which can be occupied in each localization- and spin-distinct LL state, is the area of the reduced first Brillouin zone.

Each LL wavefunction is characterized by the subenvelope functions on the different lattices with the sp^3 orbitals and spin configurations. The subenvelope functions are well-behaved in their spatial distributions, with a normal zero-point number and spatial symmetry or anti-symmetry about the localization center. Furthermore, they are similar to those of a harmonic oscillator. For the first group of LLs, the 1/6 (4/6) states can be regarded as the 2/6 (5/6) states under the interchange of two sublattices. The 2/6 states, as shown in Fig. 3(b), are chosen to illustrate the main features of the LL wavefunctions. Apparently, the subenvelope functions of the $5p_z$ orbitals (black curves) dominate the spatial distributions where the odd- and even-indexed A (B) sublattices have a similar quantum mode. Since the wavefunctions of the first valence and conduction LLs are mainly determined by the B sublattice, its zero-point number can characterize a quantum number. The $n_K^{c,v} > 0$ LLs are composed of the spin-down and spin-up configurations. For the valence LLs with small n_K^v 's, $B_{o\downarrow}$ has a much larger weight compared to $A_{o\downarrow}$. The difference between the weights declines with an increase of n_K^v and becomes negligible at $n_K^v > 20$. Also, the conduction LLs behave similarly, except that the weight of $A_{o\downarrow}$ is stronger than that of $B_{o\downarrow}$. These facts reflect the non-equivalence of the A and B sublattices in the vicinity of the K point. The degenerate \downarrow - and \uparrow -dominated LL wavefunctions resemble each other under the interchange of the weights of A and B sublattices. Specifically, the $n_{K,K'}^c = 0$ ($n_{K,K'}^v = 0$) LLs with four-fold degeneracy are spin-polarized because V_{SOC} breaks the spin

degeneracy. In addition, the K and K' points make the same contribution.

The second group is in sharp contrast to the first one regarding the main features of the LL wavefunctions, including the orbital contributions, weights of spin-up and spin-down components, and quantum modes on the A and B sublattices. The spin-split LLs present almost identical $5p_x$ - and $5p_y$ -orbital subenvelope functions with the same zero-point number on different sublattices (red and green curves in Fig. 3(d)), defined as the quantum number $n_{\Gamma\uparrow\downarrow}^{c,v}$. For the $n_{\Gamma\uparrow}^v$ ($n_{\Gamma\downarrow}^v$) LLs, the ratio of the \uparrow - to \downarrow -dependent components (\downarrow - to \uparrow -dependent ones) is about three. However, the $n_{\Gamma\uparrow}^c$ and $n_{\Gamma\downarrow}^c$ LL wavefunctions are, respectively, governed by the \uparrow - and \downarrow -dependent components, leading to the larger LL splitting. As a result of the hexagonal lattice, the nearest-neighbor atomic interactions near the Γ point are roughly proportional to k^2 . The A and B sublattices present the same quantum mode after magnetic quantization. However, the quantized electronic states near the K or K' point are associated with the linear k -dependence of the nearest-neighbor interactions, so that the difference of quantum modes on the two sublattices is ± 1 .

The low-lying LLs present an unusual B_z -dependent energy spectrum, as clearly shown in Fig. 4(a). The first- and second-group LLs frequently and exclusively cross one another (black and red curves), since they have different localization centers. The B_z -dependent energies directly reflect the zero-field energy bands, especially for the linear and parabolic bands. The former have roughly $\sqrt{B_z}$ -dependent energies, except for the $n_{K,K'}^{c,v} = 0$ LLs, which have constant energies. However, the B_z -dependence of the latter is approximately linear. With the increment of B_z , the energy spacing between the $n_{\Gamma\downarrow}^c$ and $n_{\Gamma\uparrow}^c$ LLs grows, arising from the enhanced V_{SOC} by the more localized LL wavefunctions. In addition, the energy gap slightly increases because of the variation in the $n_{\Gamma\downarrow}^v = 0$ LL spectrum. The

important differences between two groups of LLs are clearly revealed in the density of states (DOS) (Fig. 4(b)). The single- and double-peak structures come from the first- and second-group LLs, respectively. They appear at the different energy ranges, with the former having larger peak spacings. The peak height is determined by the number of degenerate states. The intensity of the single-peak structures related to the $n_{\mathbf{K},\mathbf{K}'}^{c,v} = 0$ ($n_{\mathbf{K},\mathbf{K}'}^{c,v} > 0$) LLs is two (four) times higher than that of the double-peak ones.

The magneto-electronic properties are diversified by a perpendicular electric field. The V_z -dependent energy spectrum, shown in Fig. 5(a), presents non-monotonous dispersion relations for the first group, but monotonous ones for the second group. The K-valley- and K'-valley-dependent LLs are further split by the destruction of the mirror symmetry. The two splitting LLs have an opposite V_z -dependence before V_z reaches the critical potential ($V_c \sim 147$ meV) corresponding to the linear bands intersecting at the K (K') point (blue curves in the inset of Fig. 5(a)). With a further increase of V_z , all LLs move gradually away from E_F . As to the second group, the weight of the B sublattice is enhanced by V_z , and thus the valence LL energies are reduced. The complicated V_z -dependences result in many LL crossings and certain LL anti-crossings. In addition to the intergroup LL crossings, the former come from intragroup LLs with distinct quantum modes, e.g., the direct crossing of the $n_{\mathbf{K}'}^v = 1$ and 2 LLs (arrows in Fig. 5(b)). Moreover, the intragroup LL anti-crossings only occur for the $n_{\mathbf{K}}^v$ and $n_{\mathbf{K}}^v \pm 1$ valence LLs, as well as the $n_{\mathbf{K}'}^c$ and $n_{\mathbf{K}'}^c \pm 1$ conduction LLs (blue rectangles in Fig. 5(a)). The V_z -dependent energy spectrum directly reflects the band structures at different V_z 's in the absence of a magnetic field.

There exist dramatic changes in the spatial distributions during the LL anti-crossing, as illustrated by the $n_{\mathbf{K}}^v = 1$ and 2 LLs in the range of $20 \text{ meV} \leq V_z \leq 60 \text{ meV}$ (purple and green

triangles in Fig. 5(b)). At small V_z' s, the $5p_z$ -orbital subenvelope functions of the $n_K^v = 1$ LL possess large and small weights on the $(A_{o\downarrow}, B_{o\downarrow})$ and $(A_{o\uparrow}, B_{o\uparrow})$ sublattices, respectively (Fig. 5(c)). Although the $(5p_x, 5p_y)$ -orbital subenvelope functions possess small weights, they play an important role in the process of LL anti-crossings. The intra-atomic V_{SOC} between the $5p_z$ and $(5p_x, 5p_y)$ orbitals induces a probability distribution transfer between $A_{o\downarrow}$ and $A_{o\uparrow}$ ($B_{o\downarrow}$ and $B_{o\uparrow}$). Furthermore, the electric field leads to a similar transfer between the A and B sublattices. By means of the cooperation relationship of the electric field and V_{SOC} , the weights of the $(A_{o\downarrow}, B_{o\downarrow})$ and $(A_{o\uparrow}, B_{o\uparrow})$ sublattices become comparable when LL anti-crossings take place. On the other hand, the $5p_z$ -orbital subenvelope functions of the $n_K^v = 2$ LL exhibit quantum modes identical to those of the $n_K^v = 1$ LL, except for the interchange of the weights of spin-up and spin-down configurations (Fig. 5(d)). At $V_z \sim 40$ meV, the $n_K^v = 1$ and 2 LLs are forbidden to have the same energy since their subenvelope functions are almost identical. With a further increase of V_z , the relationship between the electric field and V_{SOC} turns into a competing one. As a result, the two LLs recover to the distinct quantum modes at $V_z \geq 55$ meV. Similar anti-crossings can also be observed in the conduction LLs. Additionally, in the coexistent LL crossing and anti-crossing (Fig. 5(b)), two double peaks in DOS are changed into three single peaks, or vice versa (not shown).

The V_z -dependent LL energy spectra of silicene, germanene and tinene are quite different, as shown in Figs. 6(a) and 6(b) at $B_z = 14$ T. The low-lying second-group LLs are absent in the former two due to the weaker sp^3 bonding; that is, the low-energy magnetic quantization is mainly determined by the π -electronic states near the K and K' valleys. Their energy spacings, like in graphene, are proportional to the Fermi velocity ($v_F = 3bV_{pp\pi}/2$). Since silicene has the largest v_F and the weakest V_{SOC} , neither the LL

crossings nor the anti-crossings are induced during a variation of V_z . However, germanene presents intragroup LL crossings and anti-crossings similar to those of tinene. The anti-crossings occur at larger electric fields and exist in a wider range; they are attributed to the smaller V_{SOC} (0.196 eV) and the different sp^3 bondings.

STS measurements, in which the tunneling conductance (dI/dV) is approximately proportional to DOS and directly reflects its special structures, can provide an efficient way to identify the energy spectra under external magnetic and electric fields. This method has been successfully used to investigate the magneto-electronic energy spectra of graphene-related systems, including the $\sqrt{B_z}$ -dependent LL energies in monolayer graphene,^{27,28} the linear B_z -dependence in AB bilayer graphene,^{28,34} the coexistent $\sqrt{B_z}$ - and B_z -dependences in ABA trilayer graphene,³⁵ the absence of a simple B_z -dependence in twisted bilayer graphene,³⁴ and the bulk and layer properties of the Landau subbands in graphite.^{36,37} Moreover, the electric-field-induced energy gaps are confirmed in AB-bilayer and ABC-trilayer graphenes.^{38–40} The main features of the magneto-electronic properties of monolayer tinene—two groups of LLs, the B_z - and V_z -dependent splittings, and the intragroup crossings and anti-crossings—can be further investigated with STS. The STS measurements on the structure, energy range, spacing and intensity of the prominent DOS peaks can verify the complex sp^3 bonding, the critical spin-orbital interaction, and the cooperative or competitive relationship between V_{SOC} and V_z .

IV. SUMMARY AND CONCLUSIONS

The novel magnetic quantization in monolayer tinene, being closely related to the sp^3 bonding, spin-orbital coupling, and the influence of magnetic and electric fields, is in-

investigated by the generalized tight-binding model. The rather large Hamiltonian matrix is built from the tight-binding functions of the different sublattices, atomic orbitals and spin configurations. It has complex elements due to the special relations among the sp^3 orbitals and can be solved by using an exact diagonalization method. The two groups of feature-rich LLs, which are, respectively, dominated by the $5p_z$ orbitals and $(5p_x, 5p_y)$ orbitals, are revealed near the Fermi level simultaneously. The important differences between them lie in their spatial distributions, state degeneracy, spin configurations, and B_z - and V_z -dependence. There are approximate formulas in the B_z -dependent energy spectra, but not in the V_z -dependent ones. The LL splittings in the first and second groups are induced by the effects of electric and magnetic fields, respectively. Specifically, only the $5p_z$ -dominated group exhibits the LL anti-crossings during the variation of V_z , arising from the cooperation relationship between the electric field and spin-orbital coupling. These unique magneto-electronic properties in tinene are absent in graphene, silicene and germanene. The predicted magneto-electronic energy spectra could be directly verified by STS measurements.

ACKNOWLEDGMENT

Acknowledgments. This work was supported by the NSC of Taiwan, under Grant No. NSC 102-2112-M-006-007-MY3.

References

- [1] Novoselov, K. S.; Geim, A. K.; Morozov, S. V.; Jiang, D.; Zhang, Y.; Dubonos, S. V.; Grigorieva, I. V.; Firsov, A. A. *Science* **2004**, 306, 666-669.
- [2] Zhang, Y.; Tan, Y.-W.; Stormer, H. L.; Kim, P. *Nature* **2005**, 438, 201-204.
- [3] Nair, R. R.; Blake, P.; Grigorenko, A. N.; Novoselov, K. S.; Booth, T. J.; Stauber, T.; Peres, N. M. R.; Geim, A. K. *Science* **2008**, 320, 1308.
- [4] Sun, Z.; Hasan, T.; Torrisi, F.; Popa, D.; Privitera, G.; Wang, F.; Bonaccorso, F.; Basko, D. M.; Ferrari, A. C. *ACS Nano* **2010**, 4, 803-810.
- [5] Berciaud, S.; Ryu, S.; Brus, L. E.; Heinz, T. F. *Nano Lett.* **2009**, 9, 346-352.
- [6] Scarpa F.; Adhikari S.; Phani A. S. *Nanotechnology* **2009**, 20, 065709-65719.
- [7] Li T.; Eugenio C.; Daniele C.; Carlo G.; Marco F.; Madan D.; Alessandro M.; Deji, A. *Nat. Nanotech.* **2015** 10, 227-231.
- [8] Dávila, M. E.; Xian, L.; Cahangirov, S.; Rubio, A.; Lay, G. L. *New J. Phys.* **2014**, 16, 095002.
- [9] Zhu, F. F.; Chen, W. J.; Xu, Y.; Gao, C. L.; Guan, D. D.; Liu, C. H.; Qian, D.; Zhang, S. C.; Jia, J. F. *Nat. Mater.* **2015**, 14, 1020-1025.
- [10] Tabert, C. J.; Nicol, E. J. *Phys. Rev. B: Condens. Matter Mater. Phys.* **2013**, 88, 085434.

- [11] Tabert, C. J.; Nicol, E. J. *Phys. Rev. Lett.* **2013**, 110, 197402. (2013)
- [12] Tsaran, V. Y.; Sharapov, S. G. *Phys. Rev. B: Condens. Matter Mater. Phys.* **2014**, 90, 205417.
- [13] Matthes, L.; Pulci, O.; Bechstedt, F.; *New J. Phys.* **2014**, 16, 105007.
- [14] Liu, C. C.; Feng, W. X.; Yao, Y. G. *Phys. Rev. Lett.* **2011**, 107, 076802.
- [15] Xu, Y.; Yan, B. H.; Zhang, H. J.; Wang, J.; Xu, G.; Tang, P.; Duan, W. H.; Zhang, S. C. *Phys. Rev. Lett.* **2013**, 111, 136804.
- [16] Ezawa, M. *Phys. Rev. Lett.* **2012**, 109, 055502.
- [17] Tsai, W. F.; Huang, C. Y.; Chang, T. R.; Lin, H.; Jeng, H. T.; Bansil, A. *Nat. Commun.* **2013**, 4, 1500.
- [18] Schwierz, F. *Nat. Nanotech.* **2010**, 5, 487-496.
- [19] Vogt P.; Padova P. D.; Quaresima C.; Avila J.; Frantzeskakis E.; Asensio M. C.; Resta A.; Ealet B.; Lay, G. L. *Phys. Rev. Lett.* **2012**, 108, 155501.
- [20] Aufray, B.; Kara, A.; Vizzini, S.; Oughaddou, H.; Landri, C.; Ealet, B.; Lay, G. L. *Appl. Phy. Lett.* **2010**, 96, 183102.
- [21] Li, L. F.; Lu, S. Z.; Pan, J. B.; Qin, Z. H.; Wang, Y. Q.; Wang, Y. L.; Cao, G. Y.; Du, S. X.; Gao, H. J. *Adv. Mater.* **2014**, 26, 4820-4828.
- [22] Derivaz, M.; Dentel, D.; Stephan, R.; Hanf, M. C.; Mehdaoui, A.; Sonnet, P.; Pirri, C. *Nano Lett.* **2015**, 15, 2510-2516.

- [23] Lai, Y. H.; Ho, J. H.; Chang, C. P.; Lin, M. F. *Phys. Rev. B: Condens. Matter Mater. Phys.* **2008**, 77, 085426.
- [24] Huang, Y. K.; Chen, S. C.; Ho, Y. H.; Lin, C. Y.; Lin, M. F. *Sci. Rep.* **2014**, 4, 7509-7519.
- [25] Lin, C. Y.; Wu, J. Y.; Ou, Y. J.; Chiu, Y. H.; Lin, M. F. *Phys. Chem. Chem. Phys.* **2015**, 17, 26008-26035.
- [26] Liu, C. C.; Jiang, H.; Yao, Y. G. *Phys. Rev. B: Condens. Matter Mater. Phys.* **2011**, 84, 195430.
- [27] Li, G. H.; Luican, A.; Andrei, E. Y. *Phys. Rev. Lett.* **2009**, 102, 176804.
- [28] Miller, D. L.; Kubista, K. D.; Rutter, G. M.; Ruan, M.; Heer, W. A. D.; First, P. N.; Stroscio, J. A.; *Science* **2009**, 324, 924-927.
- [29] Deacon, R. S.; Chuang, K. C.; Nicholas, R. J.; Novoselov, K. S.; Geim, A. K. *Phys. Rev. B: Condens. Matter Mater. Phys.* **2007** 76, 081406(R).
- [30] Rutter, G. M.; Jung, S.; Klimov, N. N.; Newell, D. B.; Zhitenev, N. B.; Stroscio, J. A.; *Nat. Phys.* **2011** 7, 649-655.
- [31] Chadi, D. J. *Phys. Rev. B: Condens. Matter Mater. Phys.* **1977**, 16, 790.
- [32] Cardona, M.; Shaklee K. L.; Pollak, F. H. *Phys. Rev.* **1976**, 154 696.
- [33] Shyu, F. L.; Lin, M. F. *J. Phys. Soc. Jpn.* **2002**, 71, 1820-1823.
- [34] Luican, A.; Li, G. H.; Reina, A.; Kong, J.; Nair, R. R.; Novoselov, K. S.; Geim, A. K.; Andrei, E. Y. *Phys. Rev. Lett.* **2011**, 106, 126802.

- [35] Yin, L. J.; Li, S. Y.; Qiao, J. B.; Nie, J. C.; He, L. Phys. Rev. B: Condens. Matter Mater. Phys. **2015**, 91, 115405.
- [36] Li G. H.; Andrei, E. Y. Nat. Phys. **2007**, 3, 623-627.
- [37] Matsui, T.; Kambara, H.; Niimi, Y.; Tagami, K.; Tsukada, M.; Fukuyama, H. Phys. Rev. Lett. **2005**, 94, 226403.
- [38] Yankowitz, M.; Wang, F. L.; Lau, C. N.; LeRoy, B. J. Phys. Rev. B: Condens. Matter Mater. Phys. **2013**, 87, 165102.
- [39] Xu, R.; Yin, L. J.; Qiao, J. B.; Bai, K. K.; Nie, J. C.; He, L. Phys. Rev. B: Condens. Matter Mater. Phys. **2015**, 91, 035410.
- [40] Hattendorf, S.; Georgi, A.; Liebmann, M.; Morgenstern, M. Surf. Sci. 2013, 610 53-58

Figure captions

Figure 1. (a) The (x,y) -plane projection of monolayer tinene with a rectangular unit cell in $B_z \hat{z}$, (b) the $(5p_x, 5p_y, 5p_z, 5s)$ orbitals, and (c) the π and σ bondings.

Figure 2. (a) The valence and conduction bands along the high symmetry points (green curves) and those (black curves) without the spin-orbital interactions. Their state probabilities due to various orbitals located at two sublattices with spin-up and spin-down arrangements are, respectively, displayed in (b) and (c).

Figure 3. As for the K point, (a) the LL energies and (b) the probabilities of the subenvelope functions near the localization center in a rectangular unit cell at $B_z=14$ T. Similarly, (c) and (d) correspond to the Γ point.

Figure 4. (a) The magnetic-field-dependent energy spectra of the first and second groups (black and red curves), and (b) density of states at $B_z=14$ T.

Figure 5. The gate-voltage-dependent energy spectrum at $B_z=14$ T, and (b) the LL crossings and anti-crossing within a certain range of E^v , in which the evolution of distribution probabilities of subenvelope functions during the intragroup anti-crossing is revealed in (c) and (d). The Fermi level is indicated by the dashed red curve. Also shown in the inset of (a) is the band structure at $B_z=0$ and a critical V_z .

Figure 6. Same plot as Fig. 5(a), but shown for (a) silicene and (b) germanene.

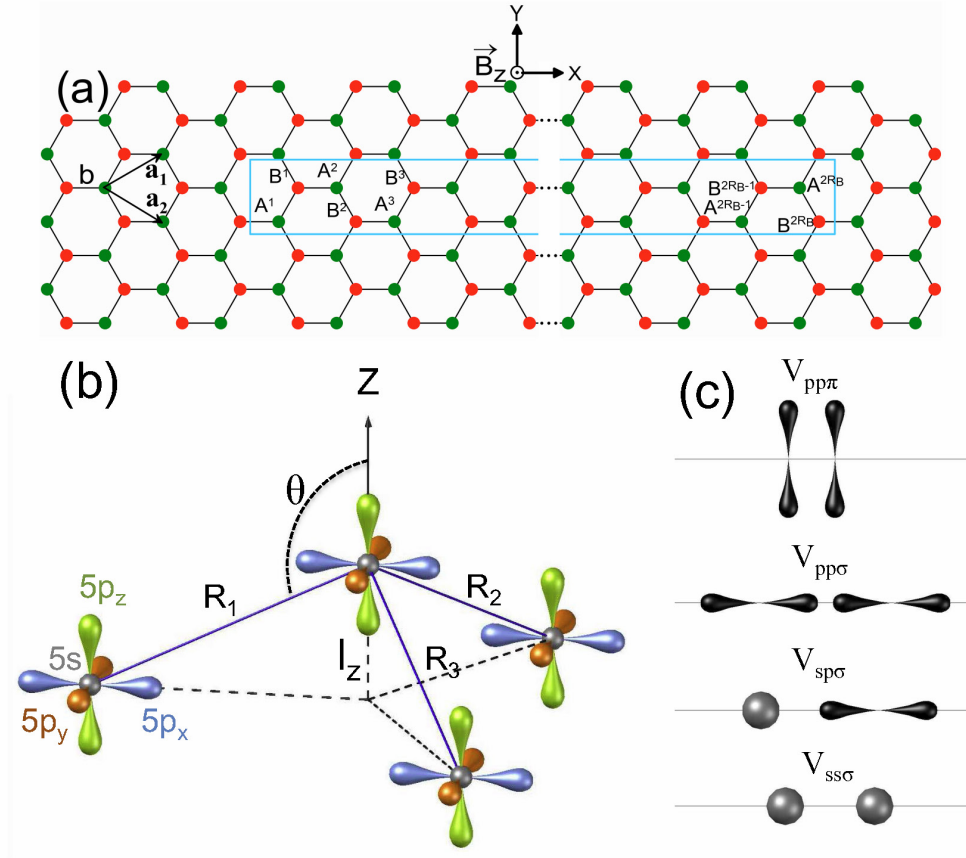


Figure 1: (a) The (x,y) -plane projection of monolayer tinene with a rectangular unit cell in $B_z \hat{z}$, (b) the $(5p_x, 5p_y, 5p_z, 5s)$ orbitals, and (c) the π and σ bondings.

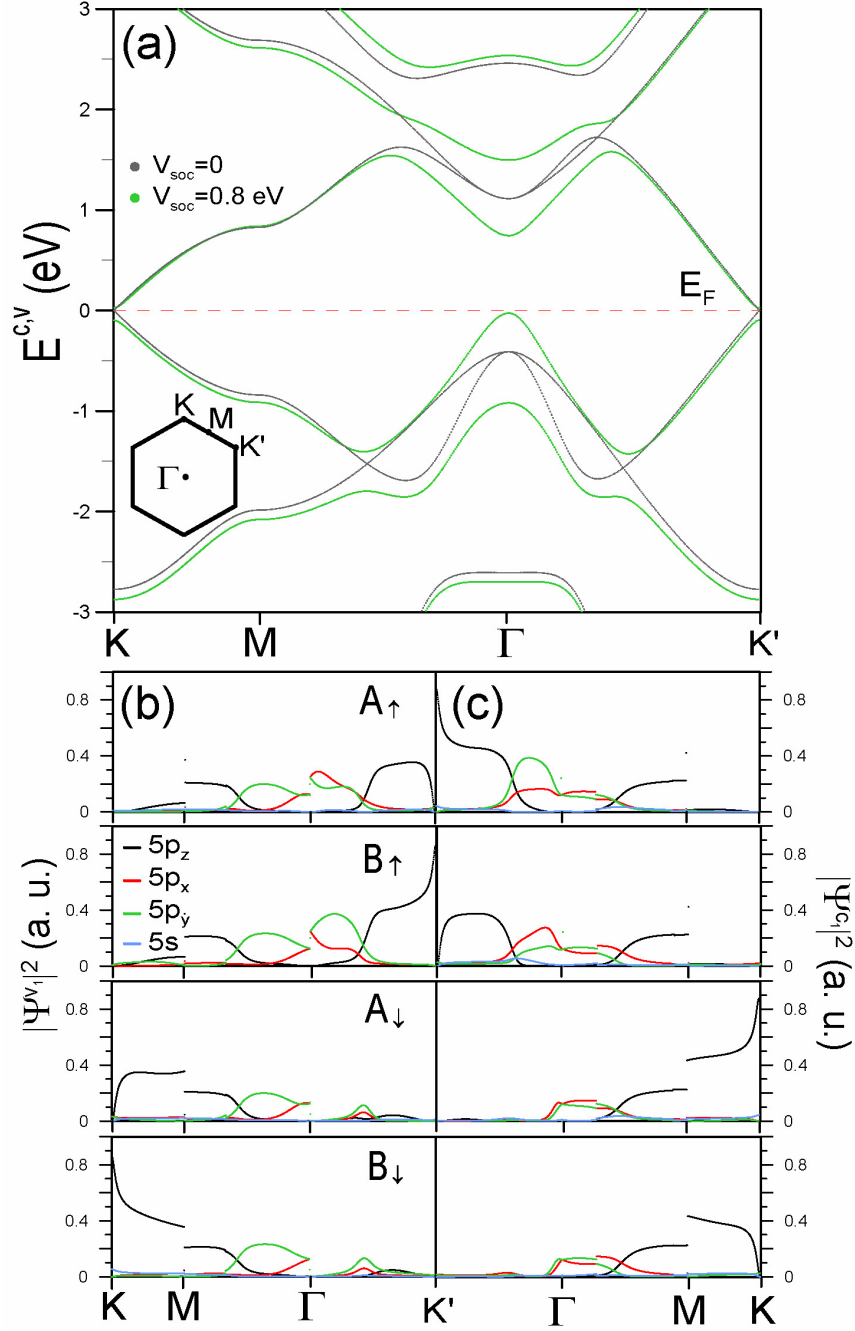


Figure 2: (a) The valence and conduction bands along the high symmetry points (green curves) and those (black curves) without the spin-orbital interactions. Their state probabilities due to various orbitals located at two sublattices with spin-up and spin-down arrangements are, respectively, displayed in (b) and (c).

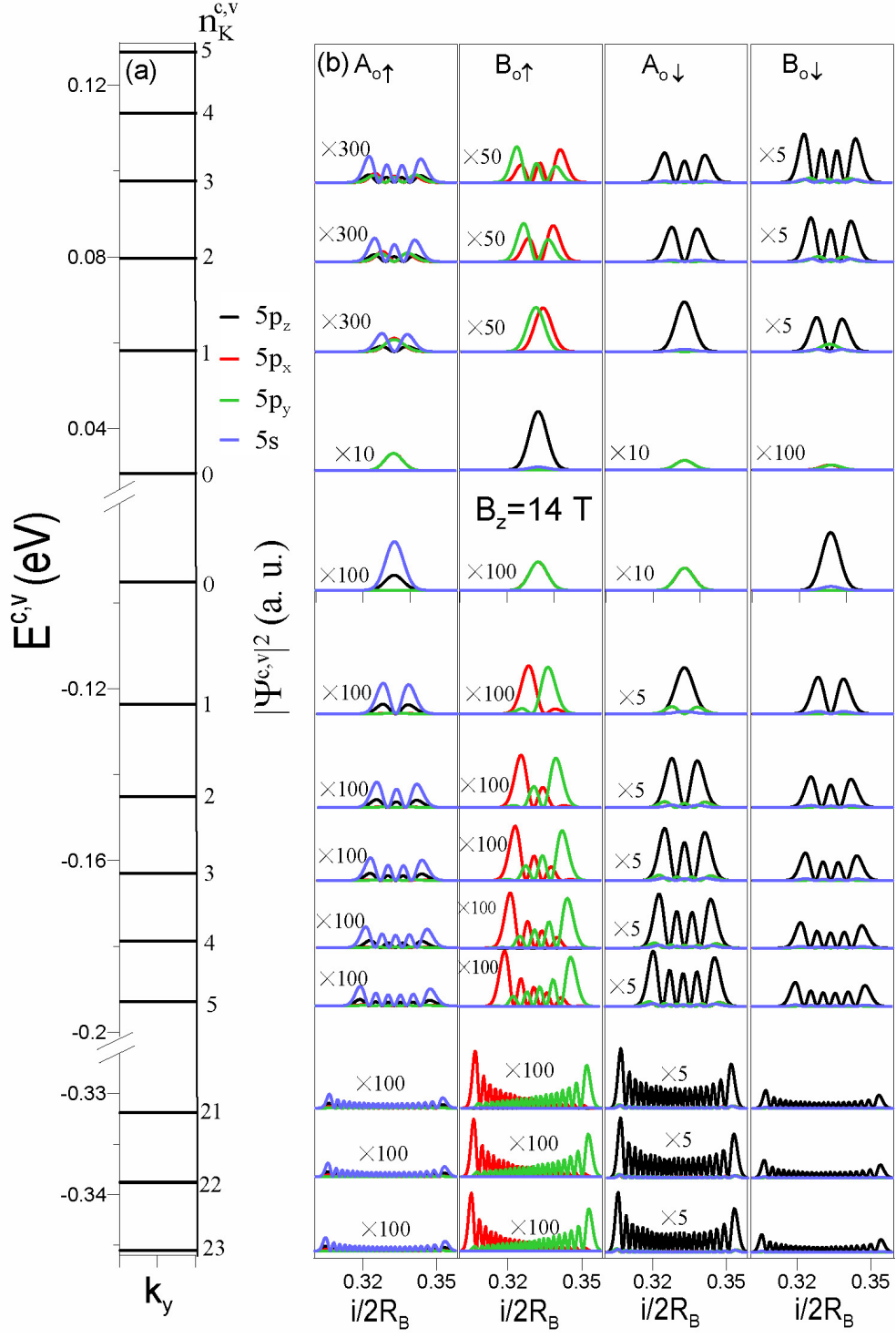
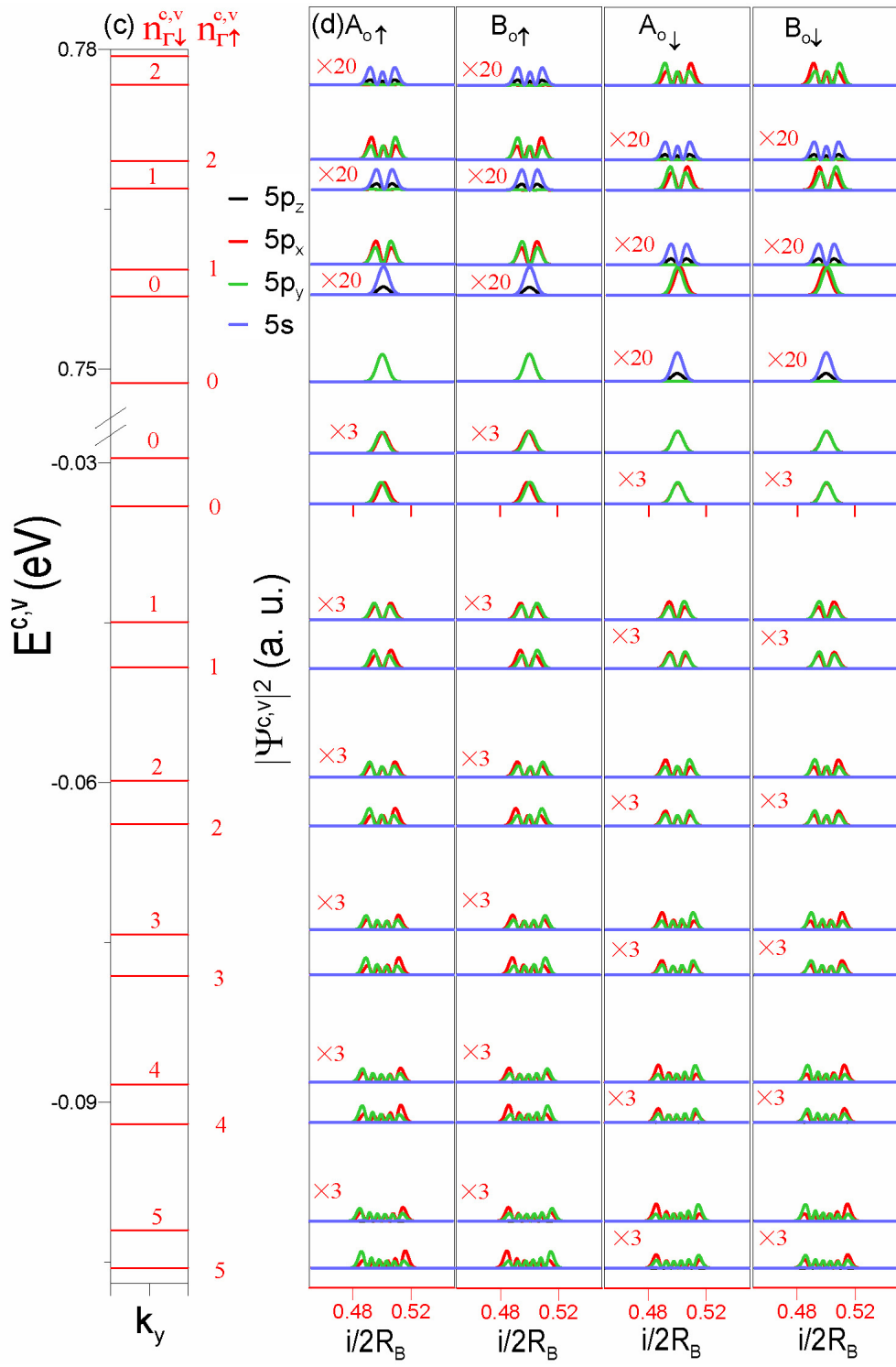


Figure 3: As for the K point, (a) the LL energies and (b) the probabilities of the subenvelope functions near the localization center in a rectangular unit cell at $B_z=14$ T. Similarly, (c) and (d) correspond to the Γ point.



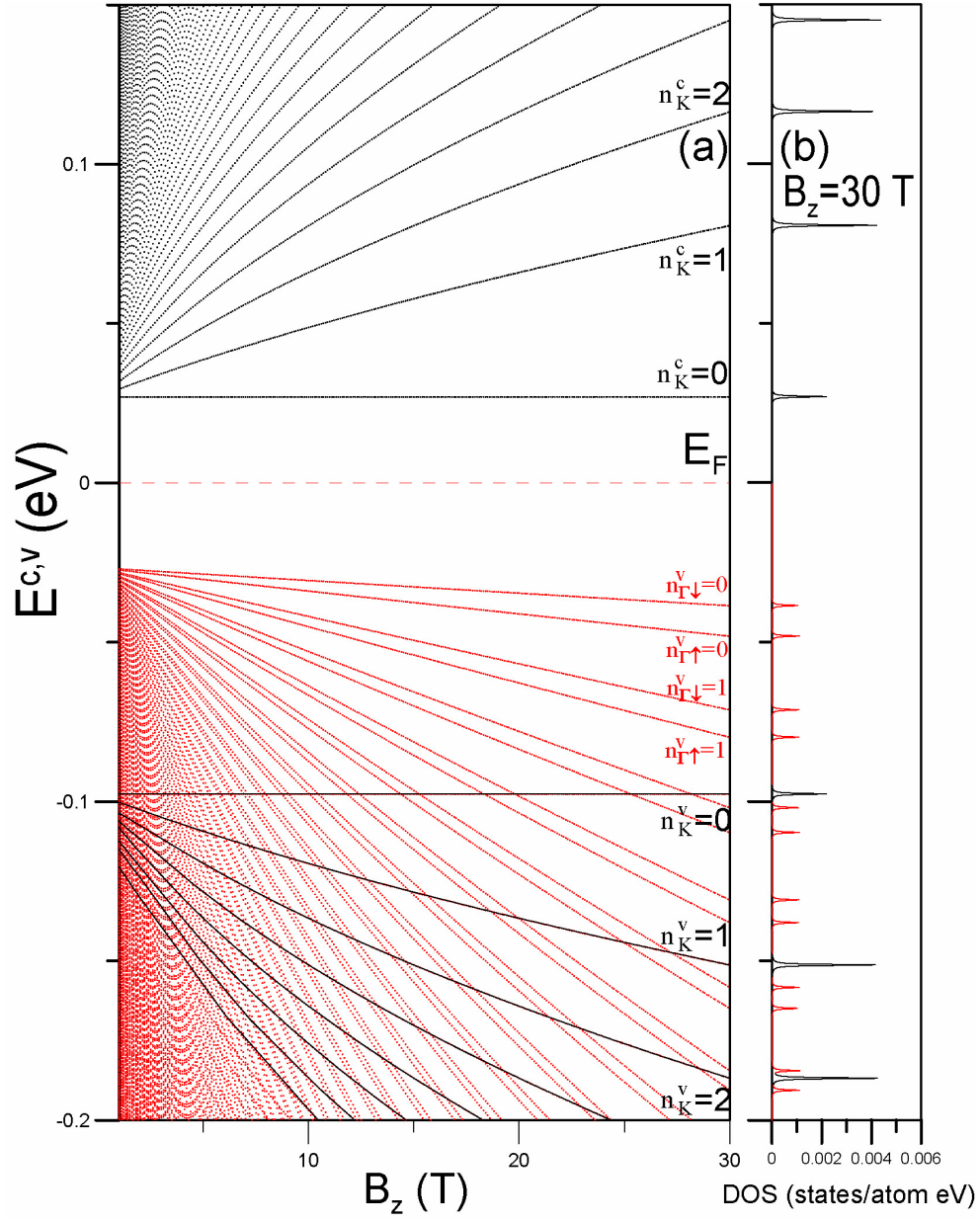


Figure 4: (a) The magnetic-field-dependent energy spectra of the first and second groups (black and red curves), and (b) density of states at $B_z=14$ T.

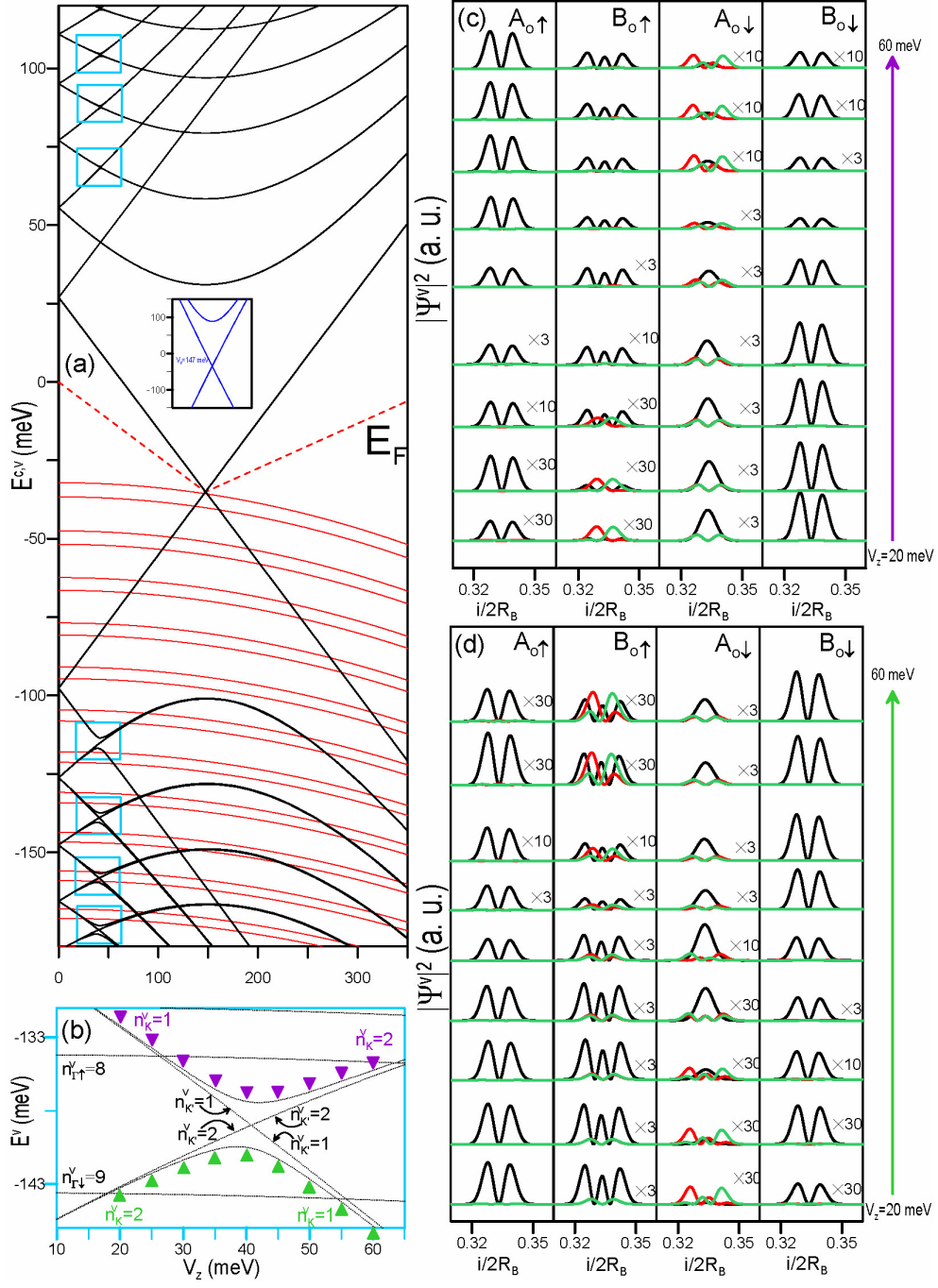


Figure 5: The gate-voltage-dependent energy spectrum at $B_z=14$ T, and (b) the LL crossings and anti-crossing within a certain range of E^v , in which the evolution of distribution probabilities of subenvelope functions during the intragroup anti-crossing is revealed in (c) and (d). The Fermi level is indicated by the dashed red curve. Also shown in the inset of (a) is the band structure at $B_z=0$ and a critical V_z .

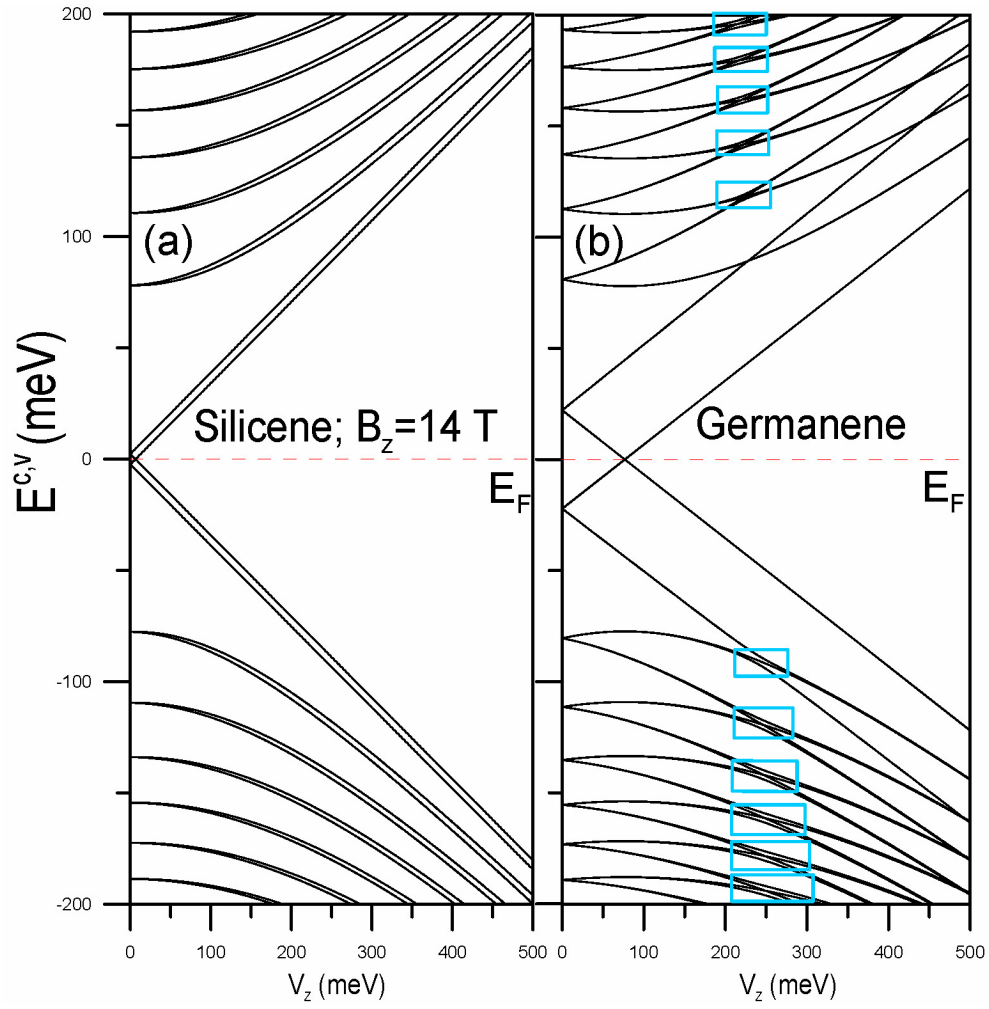


Figure 6: Same plot as Fig. 5(a), but shown for (a) silicene and (b) germanene.